PAPER • OPEN ACCESS

Modelling the sputtering and reflection from a beryllium surface: atomistic analysis

OPEN ACCESS
IOP Publishing | International Atomic Energy Agency Nuclear Fusion

Nucl. Fusion **61** (2021) 086013 (10pp) https://doi.org/10.1088/1741-4326/ac044e

Modelling the sputtering and reflection from a beryllium surface: atomistic analysis

Shokirbek Shermukhamedov[1,2], Lei Chen[1], Renat Nazmutdinov[2], Alexander Kaiser[1] and Michael Probst[1,3,*]

[1] Institute of Ion Physics and Applied Physics, University of Innsbruck, Technikerstrasse 25, 6020 Innsbruck, Austria
[2] Kazan National Technological Research University, 420015 Kazan, Republic of Tatarstan, Russian Federation
[3] School of Molecular Science and Engineering, Vidyasirimedhi Institute of Science and Technology, Rayong 21210, Thailand

E-mail: michael.probst@uibk.ac.at

Received 25 February 2021, revised 6 May 2021
Accepted for publication 24 May 2021
Published 30 June 2021

Abstract

Sputtering from plasma-facing surfaces upon particle impact can limit the lifetime of components in fusion devices, especially in the diverter region. Atomistic simulations of the processes associated with plasma–wall interactions allow for a detailed analysis of sputtering, reflection and adsorption. Most former works of beryllium sputtering by hydrogen isotopes were aimed mostly on the sputtering yield. We investigate the influence of impact energy and angle on sputtering, and analyze these quantities also for the outgoing particle. We model the sputtering by non-cumulative molecular dynamics simulations with a large number of trajectories for the various parameters. The underlying forces and energies are obtained from high-dimensional neural networks fitted to density functional calculations. We find a good agreement with the previously reported sputtering yields for perpendicular impact and a qualitative accordance with experimental data. In detail, the sputtering yield increases with increasing impact energy for angles of incidence larger than 45° with respect to the surface normal, while smaller angles show a maximal yield up to 100 eV. In cases where D reflection rather than sputtering occurs, a similar pattern is found for all angles, with the maximal reflection rate at 80°.

Keywords: plasma wall interaction, molecular dynamics, sputtering, potential energy functions, machine learning, beryllium surfaces

S Supplementary material for this article is available online

(Some figures may appear in colour only in the online journal)

1. Introduction

Erosion of plasma-facing materials (PFM) occurs under impact of energetic plasma particles. Erosion not only reduces the thickness of PFM, but also contaminates the plasma with non-fuel elements and leads to radiative losses [1–3]. Low-Z beryllium was chosen as the PFM in the first wall of ITER [4, 5]. One of the advantages of beryllium over the widely used graphite is the lower retention rate of tritium in it. However, the disadvantage of low-Z materials is the high erosion caused by sputtering under impacting hydrogen isotopes with an energy of about 100 eV [6]. Hydrogen (H, D, T) projectiles can also interact with the wall material, lose their kinetic

* Author to whom any correspondence should be addressed.

energy through successive collisions, diffuse into the material at higher temperatures or bind chemically to beryllium at lower temperatures. These retention processes also influence the blanket stability. The main concern is the activation of the wall materials by tritium, which has to be limited. In the present work, we focus on sputtering and reflection in the D/Be system. It should be mentioned that the quantification of retention and the underlying processes are typically very system-dependent. A review of newer works on the hydrogen retention in Be, C and W is given in [7]. Retention in various Be-containing materials was also discussed in chapter 3.3 of [8]. D retention and erosion of wall materials by energetic particles including H isotopes and beryllium atoms have been studied both by experiments [9–11] and computational modeling [12–22] in the past.

Sputtering is a surface sensitive process, complicated by chemical impurities on the Be surface and other factors [9]. Nishijima *et al* measured the erosion of various Be surfaces exposed to deuterium plasma with D incident energies from 10 to 140 eV in a wide temperature range of samples [10]. In a recent work, Hakola *et al* performed experiments on fuel retention in beryllium-containing films of various compositions including Be–D and Be–O–D samples. The influence of surface temperature and film thickness on retention was also reported. They obtained retention values of about 1–2 at% in co-deposits on Be–D samples [11]. Besides obtaining experimental data on the erosion on beryllium surface, understanding the mechanisms of sputtering and retention are also quite important [24]. For this purpose, traditional analytical theory, semi-empirical formulas as well as molecular dynamics (MD) and Monte Carlo (MC) methods have been used. For example, the energy dependence of the sputtering yield (defined as the ratio between incoming particles to sputtered ones) has been fitted to a variety of suitable analytical formulas dealing with various projectile nuclei and targets [12, 13]. Björkas *et al* performed MD simulations with a bond-order potential (BOP) to investigate the swift chemical sputtering of Be at deuterium impacts between 7 and 100 eV. The ratio of Be to BeD sputtering yields was found to be about 4:1 [17]. Safi *et al* investigated the dependence of impact energy and surface temperature on Be sputtering yields by MC and MD simulations. They show that the erosion yield of Be increases with the surface temperature but decreased with D concentration. For impact energies larger than 100 eV, erosion also decreases due to the deeper penetration of D [21, 22].

The interatomic potential is the crucial part in all atomistic simulations. It defines the physical properties of the simulated system. There exist several reactive potentials for the Be–H systems, for example BOP potentials which have often been used in sputtering simulations [15, 16]. Despite the fact that they are versatile many-body potential functions, they still lack in being able to fully reproduce density functional calculations. In fact, they can be seen as approximations to density functional methods [23] Behler and Parrinello's method has made the use of high dimensional neural networks potentials (NNPs) as potential energy functions versatile and universal [26]. These NNPs have shown a high accuracy of fitting DFT-derived potential energy surfaces and have already been successfully applied for many important tasks in computational material science [27–29].

In this work, we model the non-cumulative sputtering of pristine beryllium surfaces by hydrogen (D) projectiles as well as retention processes. Based on our works in [30, 31], we continue to develop neural network potential energy functions using the Behler–Parrinello approach as implemented in the *n*2*p*2 code [32, 33]. With neural networks representing the potential energy surfaces sputtering, reflection, and retention rates for various incident angles α (0°, 20°, 45°, 60° and 80°) on Be(0001) are calculated for projectiles with 10–100 eV kinetic energy.

2. NN-driven MD simulations (computational methods?)

2.1. Behler–Parrinello method

In the Behler–Parrinello approach [26], the total energy E^{pot} of a configuration is obtained as a sum of atomic energies E_i, which is the output of an atom-centered and element-specific neural network. The input to the network is the local environment of the atom. Specifically, the coordinates of neighboring atoms are converted into symmetry-invariant functions that describe the local environment. These symmetry functions are then input nodes in the neural network. We have used the same settings as in [30], a feedforward neural network topography with two hidden layers of 30 nodes each, the softplus activation function and a cut-off radius of 7 Å. The input nodes consist of radial and angular Behler-type symmetry functions [41].

The neural network potentials were optimized according to the Behler–Parrinello model described above using the *n*2*p*2 code [32, 33]. An asset of *n*2*p*2 for constructing the NNP is that both the total energies and atomic forces of the training structures are used for optimizing the weights in the fitting process. The training algorithm is a multi-stream Kalman filter that optimizes the NN weights and offsets [33]. After the NNP is created, the MD simulations are performed with a modified LAMMPS code [40].

The training set size limits the efficiency of the training process. In particular, for more than two elements, storing all symmetry function values during the training process requires vast amounts of main memory. On the other hand, with our refinement procedure, it is not unlikely to have redundant structures in the training set. Therefore, we implemented a farthest point sampling method inspired by [42] to find and sort out structures that are similar. The following distance norm was employed

$$\Delta G\left(i,j\right)=\frac{1}{n}\sum_{k=1}^{n}\left|G_{\mathrm{s}}\left(i,k\right)-G_{\mathrm{s}}\left(j,k\right)\right| \tag{1}$$

with $G_{\mathrm{s}}(i)$ being a sorted vector of all n symmetry functions of the ith structure in the training set. Only structures with the same number of atoms of each element are compared. If two structures are equal, albeit from rotations, translations or permutations of like atoms, their ΔG norm is zero. We can now

reduce the number of symmetry functions by rejecting those N structures that have the smallest values of $\min_{j>i}\Delta G(i, j)$, thus being the ones closest to some other structures in the training set in terms of symmetry functions.

2.2. Network training

2.2.1. Density functional calculations. Energies and forces from DFT calculations serve as training and test data to determine the NN parameters, both in the initial and refinement steps. One can view the NN as a 'bridge' to generate fast DFT-quality forces that drive the MD simulation.

Kohn–Sham density functional theory with the Perdew–Burke–Ernzerhof [36] functional was used for total energy calculations and for Born–Oppenheimer *ab initio* MD to generate the initial and further training data sets [34, 35]. All calculations were performed with the Vienna *Ab Initio* Simulation Package (VASP) [37, 38]. Projector augmented wave (PAW) [39] potentials for Be (with two valence electrons) from the VASP library replaced the two 1s electrons of Be. For our rather large supercell, a gamma-centered k-point mesh of $3 \times 3 \times 3$ was employed. The Kohn–Sham orbitals were expanded in a plane wave basis set with periodic boundary conditions. Spin-unpolarized calculations were performed with a cut-off energy of 350 eV [30]. The validity of PAW and the other approximations had been checked before [31]. As described below in detail, the initial set of training structures, energies and forces were obtained from sputtering trajectories with different incident angles of deuterium on small supercells. In these cells, the lowest layer of atoms in the slab was fixed while all other atoms were allowed to relax. A convergence criterion of 10^{-4} eV Å^{-1} was used for the forces in the optimization process.

2.2.2. Generation of training data and network training. In order to generate the training data, sputtering simulations were performed by using direct density functional MD simulations first, as described below. In all sputtering simulations, the projectile D atom was initially placed 5 Å above the target surface with uniformly chosen random coordinates for x and y and supplied with the initial velocity corresponding to the impact energy.

The initial training data consisted of 2400 configurations extracted from 12 *ab initio* MD trajectories, which were generated by performing *ab initio* MD simulations on a Be(0001) surface with 96 atoms. The slab geometry was first optimized, and then equilibrated for 2 ps at 300 K within the canonical ensemble using the Nosé–Hoover algorithm [43, 44]. A subsequent equilibration time of 2 ps was used to generate different initial surface coordinates for the sputtering processes. Then, the impacts of single D atoms with an energy of 100 eV were simulated without a thermostat.

We have implemented an iterative refinement protocol as shown in figure 1 in [30] to successively improve the training data. This procedure relies on the fact that the many parameters in the NNP lead to an overdetermined expression where multiple parameter sets are equally good for data reproduction and interpolation but will give different results for extrapolation, thus enabling the identification of configurations which must be incorporated into the training set. Therefore, two preliminary NNPs with the same topography but differing in their initial weights and biases were fitted to the initial training data generated from *ab initio* MD as described above. One of the fitted NNPs is then employed in short MD simulations (40 fs) of the sputtering on a beryllium surface with 96 atoms by D projectiles at energies from 8 eV to 100 eV. Next, the energies and forces of these new configurations extracted from MD trajectories are predicted by the NNP not used for the simulation. The configurations with large differences of energies or forces from different NNPs were added back to the training set after calculating their energies and forces from DFT. This new training set was then run through the sampling method described in section 2.1 to eliminate similar structures. Overall, we observed that for a system of 97 atoms the NNP-based MD simulation is about 100 000 times faster than a DFT-based one. Comparison with a bond order potential showed in turn the NNP to be ≈20 times slower.

The final reference data set consists of 8025 configurations containing 96 Be atoms and one D atom each. 7211 total energies and 2098 401 forces are used to train the final NNP. The remaining 10% of data is the test set used to validate the interpolation capacity of the potential. With 60 training steps, the RMSE in the test set converged to 4.34 meV/atom for energies and 0.81 eV Å^{-1} for atomic forces, the corresponding values in the training set are 3.16 meV/atom and 0.41 eV Å^{-1}. There was no evidence for overfitting in the training process. The range of potential energies present in the training data is quite large and their distribution is shown in figure 1S of the supplementary information (https://stacks.iop.org/NF/61/086013/mmedia).

The correlation between NNP and DFT energies per atom and the corresponding ones for the atomic forces are shown in figure 1. Only the x-components of the forces are shown for clarity. The correlation is in general very satisfactory for both energies and forces.

2.3. Sputtering simulation

The initial simulation box was created from 512 beryllium atoms in a hexagonal closed packed structure (HCP) with the (0001) surface in the z direction. The box dimensions are $x = 18$ Å, $y = 16$ Å and $z = 27$ Å. It was relaxed at 300 K in the NVT ensemble for 0.1 ps. The sputtering simulations were performed in the NVE ensemble. The D atoms as projectiles were deposited as described in section 2.2.2. The timestep was dynamically adjusted between 0.01 and 1 fs depending on the velocity of the projectile, with the step size being resampled every five steps such that no atom moved more than 0.05 Å between these five steps. The simulation proceeds until one of halting several conditions is met. These conditions involve, for example, the exit of a sputtered particle or reaching a limit of 10 000 steps. At impact energies of 10 and 20 eV, 5000 non-cumulative irradiations were simulated (2000 for all other energies). In this way, reasonable statistical information is pro-

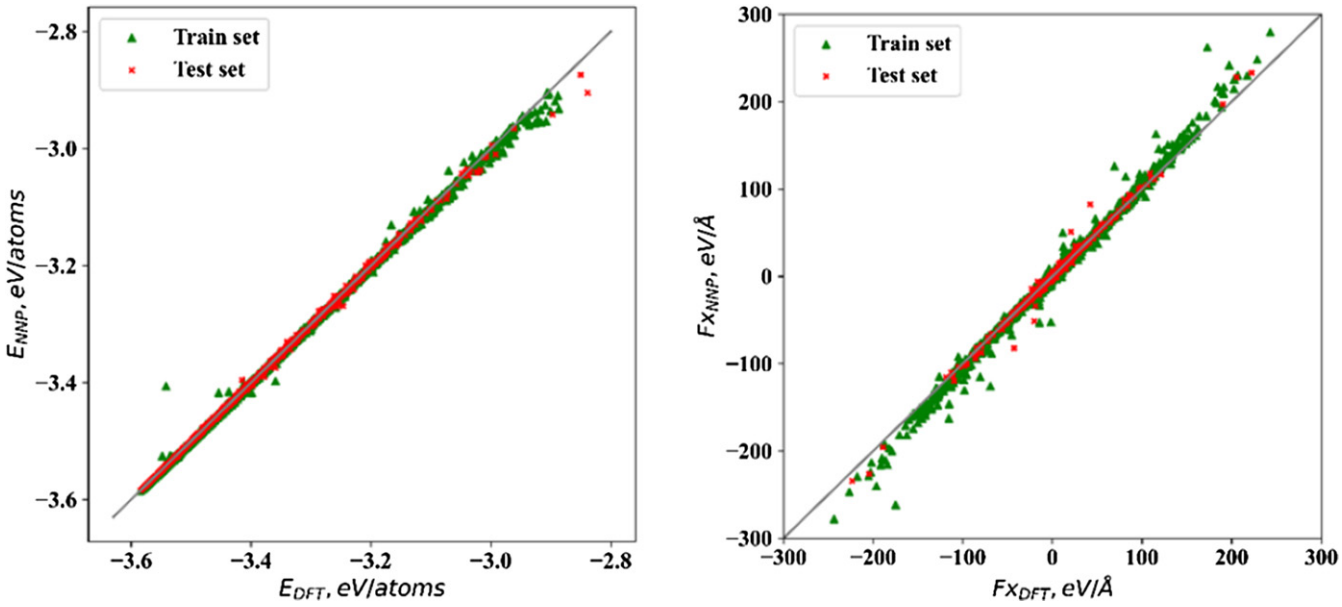

Figure 1. Correlation between NNP-derived and DFT energies (left) and between the x-components of the forces (right) for all configurations in the training and test set.

vided even for the very small sputtering yields at low impact energies. The visualizations were performed with the OVITO [45] software.

3. Sputtering yields at perpendicular impact

The main aim of our work is the analysis of trajectories with respect to angular and energetic distributions of sputtered and reflected atoms. However, we can compare the trajectories from perpendicular impact with former works. The NNP based sputtering yields together with the data from several former works are shown in figure 2, defined as sputtering of Be atoms per the total number of D impacts. We compare them with experimental data from Roth *et al* at two different temperatures and with the work of Nishijima *et al* [10] (PISCES-B measurements). At lower incident energies, our simulated yields are close to the PISCES-B data. With increasing impact energy our sputtering yields fall in between the works mentioned above. The experimental yields at 100 eV have a large spread and it is difficult to judge their accuracy, a well-known consequence of the multitude of parameters present in experimental measurements and simulations [14], both of which contain complex information about surface structure, surface temperature and several other parameters. However, we observe good agreement with other computational works. At high incident energies (50, 75 and 100 eV), our data compare well with the values from Björkas *et al* [14, 18]. At 20 eV, the NNP based sputtering yield is somewhat lower than their value. In contrast to Björkas *et al* [18], we did not encounter BeD chemical sputtering events at 20 eV. For even lower incident energy (10 eV), no sputtering was found in our sample of 5000 trajectories. The Eckstein sputtering formula was used with the parameters $E_{\text{th}} = 9.51$ eV, $q = 0.10$, $\mu = 1.99$ and $\lambda = 1.76$

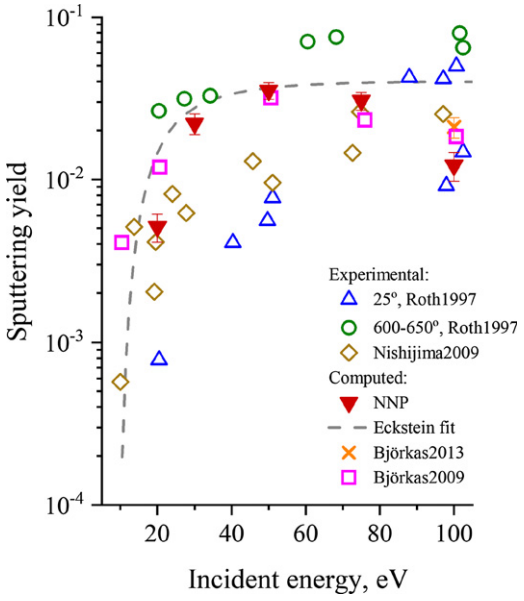

Figure 2. Sputtering yields from the irradiation of a Be(0001) surface by non-cumulative D impact with various incident energies from our simulation and from former works. The dashed line represents the Eckstein formula [13]. Experimental values are from [9, 10] and computed values are from [14, 18].

taken from [13]. Despite a good agreement between the sputtering yields from MD simulations, the experimental results do not show the decrease of around 100 eV. This feature will be discussed in section 4.1. At low incident energies chemical sputtering from the surface plays a role as well. D chemical sputtering, cumulative sputtering simulations are more appropriate [14].

Table 1. Sputtering yields with their statistical error, reflection rate and retention rate for a Be(0001) surface irradiated by D impacts obtained from MD simulations using a neural network potential.

Incident angle	Energy (eV)	10	20	30	50	75	100
$\alpha = 0^\circ$	Number of MD trajectories	5000	5000	2000	2000	2000	2000
	Be sputtering yield	0	0.005	0.022	0.035	0.031	0.012
	Statistical error Δ	—	0.001	0.003	0.004	0.004	0.002
	D reflection rate	0.12	0.19	0.20	0.17	0.11	0.04
	D retention rate	0.88	0.81	0.80	0.83	0.89	0.96
$\alpha = 20^\circ$	Number of MD trajectories	5000	5000	2000	2000	2000	2000
	Be sputtering yield	0	0.004	0.014	0.027	0.047	0.028
	Statistical error Δ	—	0.001	0.003	0.004	0.005	0.03
	D reflection rate	0.10	0.17	0.18	0.16	0.13	0.07
	D retention rate	0.90	0.83	0.82	0.84	0.87	0.93
$\alpha = 45^\circ$	Number of MD trajectories	5000	5000	2000	2000	2000	2000
	Be sputtering yield	0	0.007	0.015	0.054	0.059	0.053
	Statistical error Δ	—	0.001	0.003	0.005	0.005	0.005
	D reflection rate	0.10	0.20	0.23	0.20	0.16	0.12
	D retention rate	0.13	0.28	0.32	0.33	0.29	0.23
$\alpha = 60^\circ$	Number of MD trajectories	5000	5000	2000	2000	2000	2000
	Be sputtering yield	0	0.004	0.032	0.080	0.123	0.127
	Statistical error Δ	—	0.001	0.004	0.008	0.007	0.007
	D reflection rate	0.13	0.28	0.32	0.33	0.29	0.23
	D retention rate	0.20	0.51	0.67	0.76	0.78	0.77
$\alpha = 80^\circ$	Number of MD trajectories	5000	5000	2000	2000	2000	2000
	Be sputtering yield	0	0.005	0.015	0.035	0.050	0.059
	Statistical error Δ	—	0.001	0.003	0.004	0.005	0.005
	D reflection rate	0.20	0.51	0.67	0.76	0.78	0.77
	D retention rate	0.80	0.49	0.33	0.24	0.22	0.23

4. Energetic and angular distributions of the trajectories

4.1. Influence of the impact angle

In table 1, we report sputtering yields, reflection rates (reflection of D atoms per total impacts) and retention rates (adsorption of D per total impacts). The statistical error of the sputtering yield was estimated as $\Delta = \sigma/\sqrt{N}$, where σ is the standard deviation from assuming a Bernoulli distribution and N is the number of MD trajectories over which we average.

The sputtering yield is around 0.03 for incident energies above or equal to 50 eV and much smaller for lower ones. At 75 eV and 100 eV, we observe that the yield decreases slightly again. This feature is not present in the experimental data shown in figure 2 and the ones fitted to experiments. For them the yield starts to decrease only at higher energies not covered by us. The reason might be that the experiments sample various angles on the microscopic scale. This causes the actual perpendicular kinetic energy component of the particle to be smaller than assumed from figure 2.

We also see in figure 2 that the sputtering threshold energy E_{th} below which no sputtering occurs within 5000 trajectories lies below 20 eV. The difference between this value and a previous estimate of 9.51 eV [13] can be attributed to the very small sample of sputtering events at such low energies.

The left panel of figure 3 visualizes the sputtering process. The right panel shows the derived dependence of Be sputtering yield on various D incident angles and energies for incident energies larger than 10 eV, the sputtering yield increases from 0° to 60° and then goes down slightly.

It is well known that impacting particles cause collision cascades in the surface layers. Such cascades with light atoms can be initiated in two ways: the impacting particle only enters the surface layer (S_{I}) or the impacts are backscattered from the interior of the solid to the surface (S_{II}), respectively. The total sputtering yield is then a combination of these two parts ($S_{\mathrm{T}} = S_{\mathrm{I}} + S_{\mathrm{II}}$) [24, 25]. We can interpret the simulated sputtering in these terms. Figures 4(*a*) and (*b*) show sputtering corresponding to mechanisms S_{I} and S_{II}, respectively. The impact angle is 45° and the energy 100 eV for both examples. We find that at perpendicular impact the mechanism S_{II} dominates while with increasing impact angle, the S_{I} contribution becomes larger and the sputtering yields reach their maximal values at 60°. At large angles, reflection from the surface layer prevails. On the other hand, with increasing impact energy the penetration depth of D increases as well and the S_{II} component begins to dominate S_{T}.

4.2. Distributions of sputtered Be and reflected D

4.2.1. Be sputtering. The three-dimensional histogram in figure 5 on the left shows the angular distribution of the sputtered Be atoms for five different incident angles of D impacts at 100 eV. All histogram bars for one specific incident angle are plotted in the same color in figure 5 and range from blue for 0° to violet for 80°. Surprisingly, the shape (center and variance) of the distributions does not depend on the incident angle. Sputtering occurs between 0° and 80° with a maximum

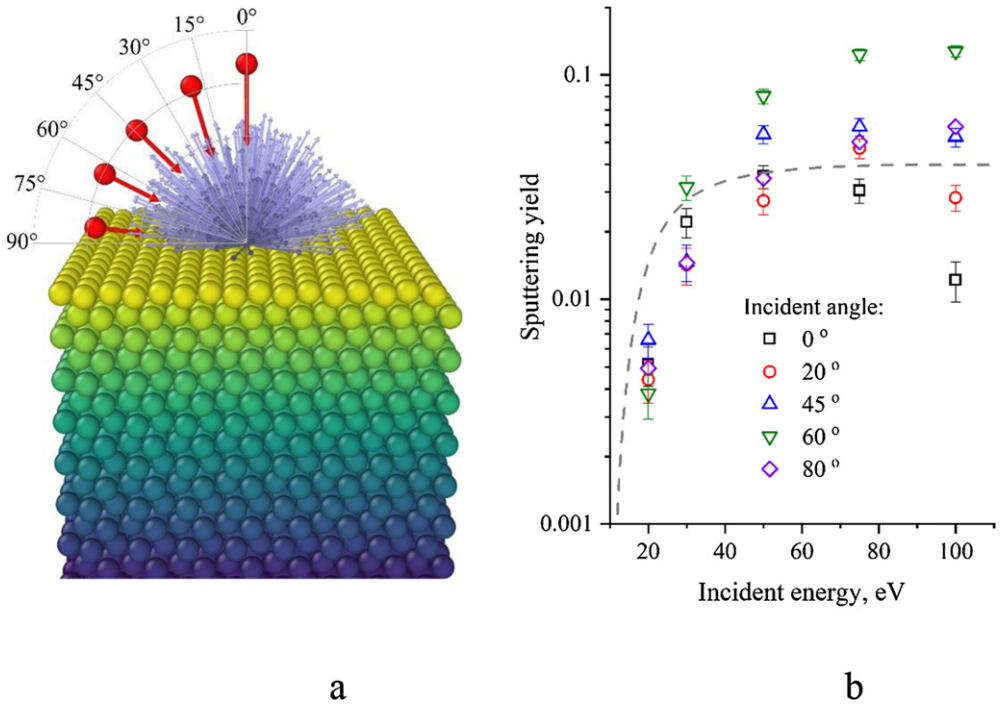

Figure 3. (*a*) Visualization of incoming D and sputtered Be atoms; (*b*) sputtering yield as function of the kinetic energy for different incident angles. The dashed line represents the Eckstein fit.

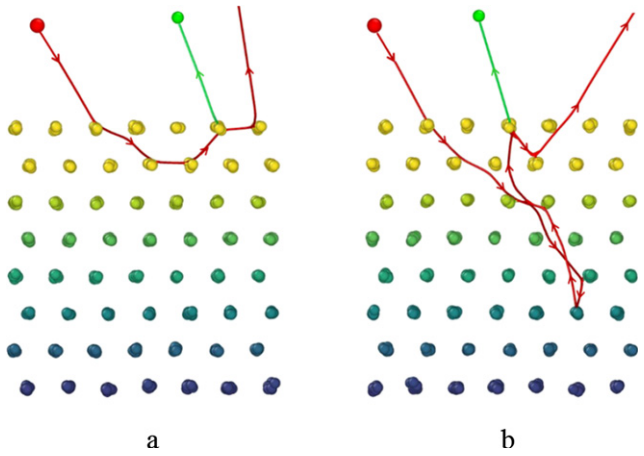

Figure 4. Sputtering trajectories for an impact angle 45° and 100 eV kinetic energy as examples for the S_{I} (*a*) and S_{II} (*b*) mechanisms. The red line corresponds to the deuterium trajectory and the green one to a sputtered Be atom.

yield of 40° to 50°. The yield itself is, however, strongly influenced by the incident angle. The largest yield is found at an incident angle of 60°. It decreases to about 50% of its value at 45–80° and to 10% at 20°.

Figure 5(*b*) shows a similar type of histogram with the impact energy instead of the incident angle, which is fixed at 60°. One can see a broad angular distribution of the sputtered Be atoms. This distribution gets narrower, again with the maxima between 40° and 50°, as the incident energy increases. A similar trend is observed for all other impact energies (figure S2).

Histograms for the other impact energies and other incident angles do not change the discussion and are shown in figures S2 and S3 of the supplementary information

4.2.2. D reflection. The reflection of D atoms competes with sputtering. In figure 6(*a*), the reflection probabilities are shown in the same way as before, with the sputtering yields as a function of the incident energy for different incident angles. The 'flat' incident angle of 80° causes by far the highest probability of reflection, which decreases regularly towards the angle approaching the surface normal. Generally, the maximal reflection probability is found at energies between 30–50 eV. With increasing incident angle, the maximum moves slightly towards higher energies. However, for an incident angle of 80° a plateau of the kinetic energy of the reflected particle at around 50 eV for all incoming energies can be seen. The lowest probability of reflection (table 1) at 100 eV incident energy is 4.4% for perpendicular D impact.

Figure 6(*b*) compares the D reflection probabilities at 100 eV with the literature data. For low energies, our values are about two times less than the values from BCA-based simulations [46, 47], while for higher energies the difference becomes less. The data indicates a maximum in the reflection probability for D impact at between 20 and 40 eV.

The decrease in reflection rate on the high energy side can be attributed to the increased probability of deposition of the projectile on or below the surface. For comparison, in MD simulations of sputtering from a beryllium-oxide surface by D impact [48], the reflection probability even decreased by one order of magnitude between 10 and 100 eV. On the low energy side, the decrease in reflection yield probably results from

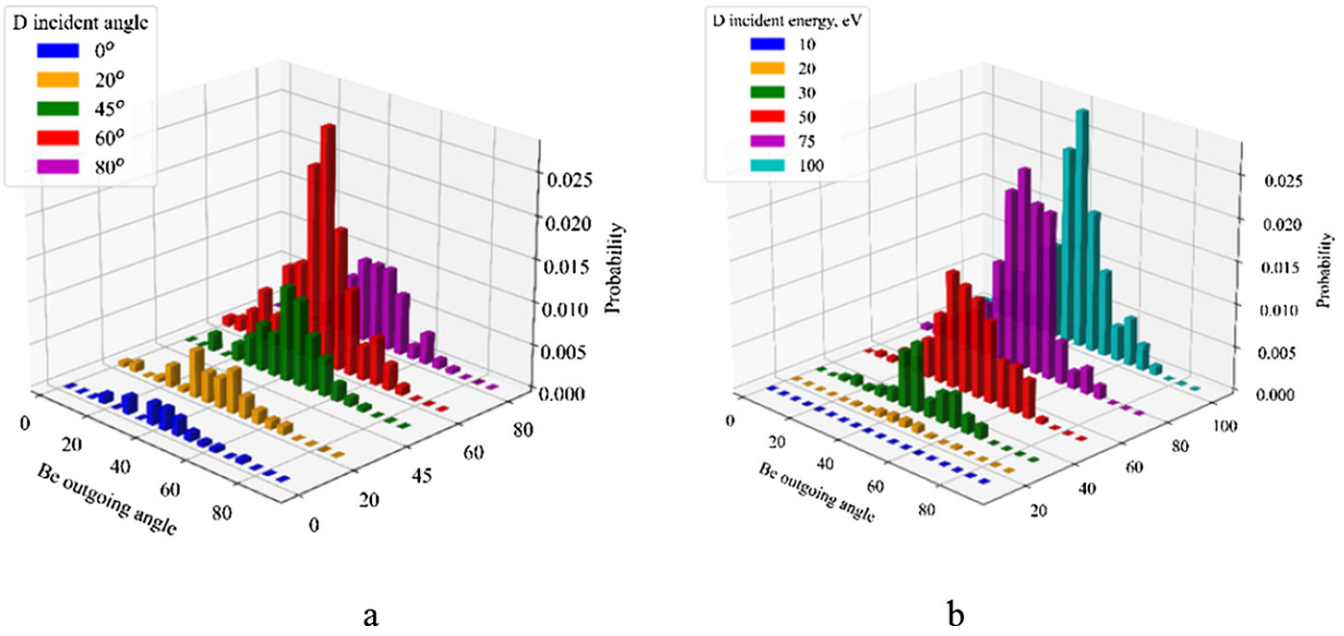

Figure 5. Histograms of the Be outgoing angle as a function of: (*a*) the D incident angles for an incident energy of 100 eV; (*b*) the incident energies with a fixed angle of 60°.

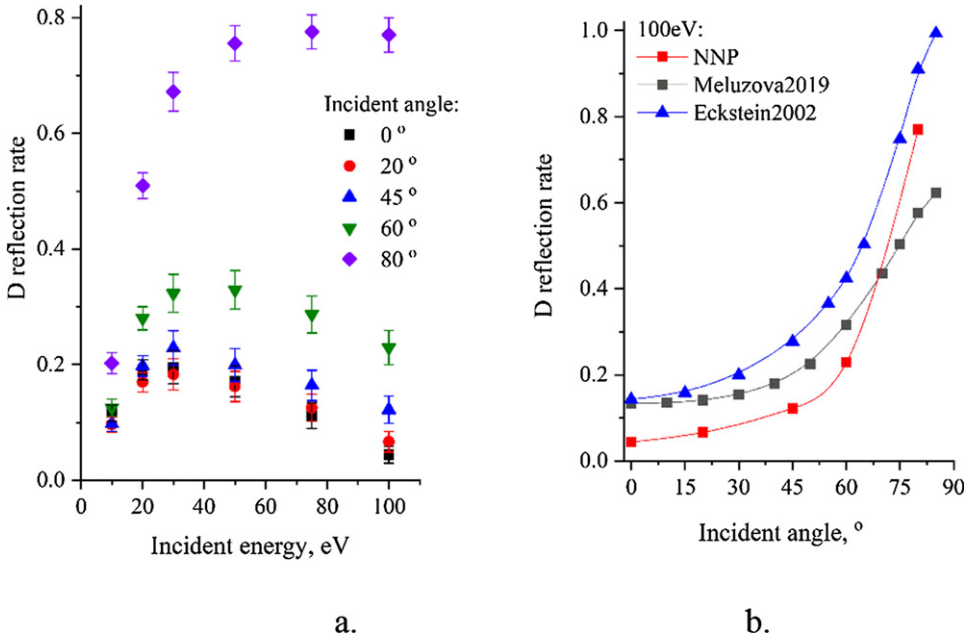

Figure 6. D reflection probabilities: (*a*) D reflection rate for different impact angles. (*b*) Comparison with data from [46, 47] at an impact energy of 100 eV.

chemisorption due to Be–D adatom binding (chemical sticking). It should be mentioned that a typical adsorption energy of H or D on a Be(0001) surface is around 2.35 eV, much smaller than the kinetic energies of the D atoms in our sputtering events [49].

Finally, we analyzed at the angular distribution of the reflected D atoms, again equivalent to the sputtering scenario. The respective histograms are shown in figure 7(*a*) for 100 eV and histograms for other energies are presented in figure S4. It is characteristic that the distributions are relatively wide for small incidence angles and that for larger incidence angles their maxima move to large angles as well, even though a large variance remains. As mentioned above, maximal reflection is found for the 80° impact angle. Figure 7(*b*) resolves the energies for this impact angle and shows angular distributions for all simulated energies at the same angle. The maxima of the D reflection probabilities are found between 60° and 80° irrespective of the incident energy. Histograms for the other incidence angles are found in figure S5 and show the same trend.

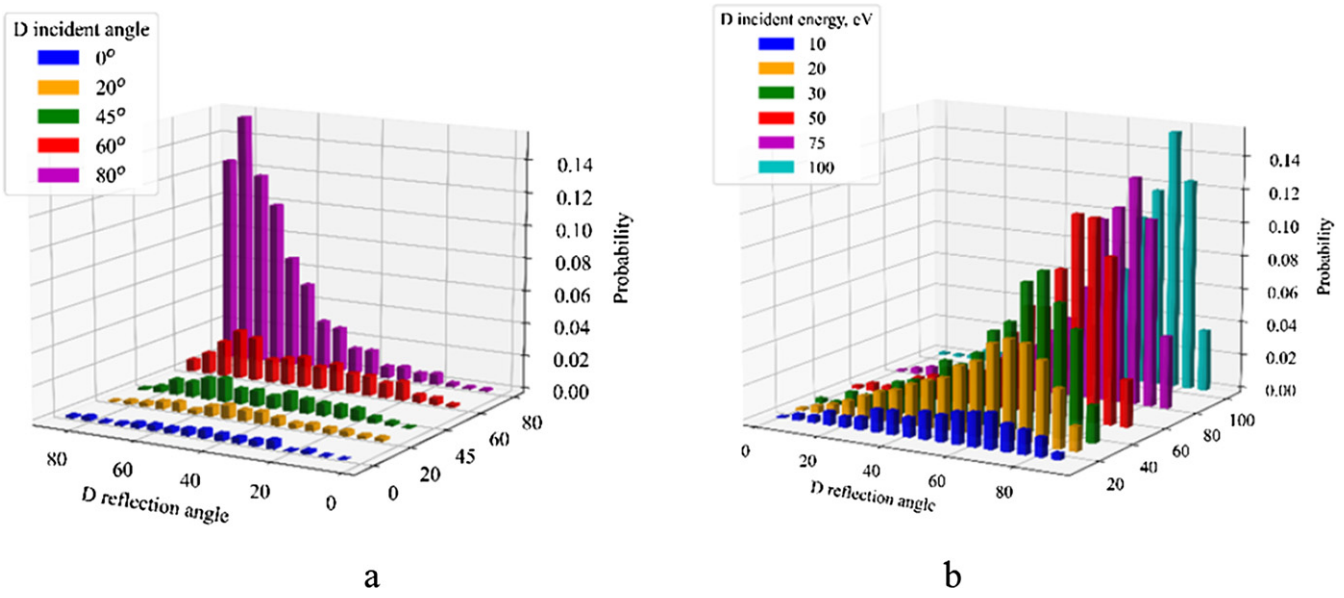

Figure 7. Histograms of D reflection probabilities: (*a*) for the different D impact angles at the 100 eV incident energy; (*b*) different energies at the fixed impact angle of 80°.

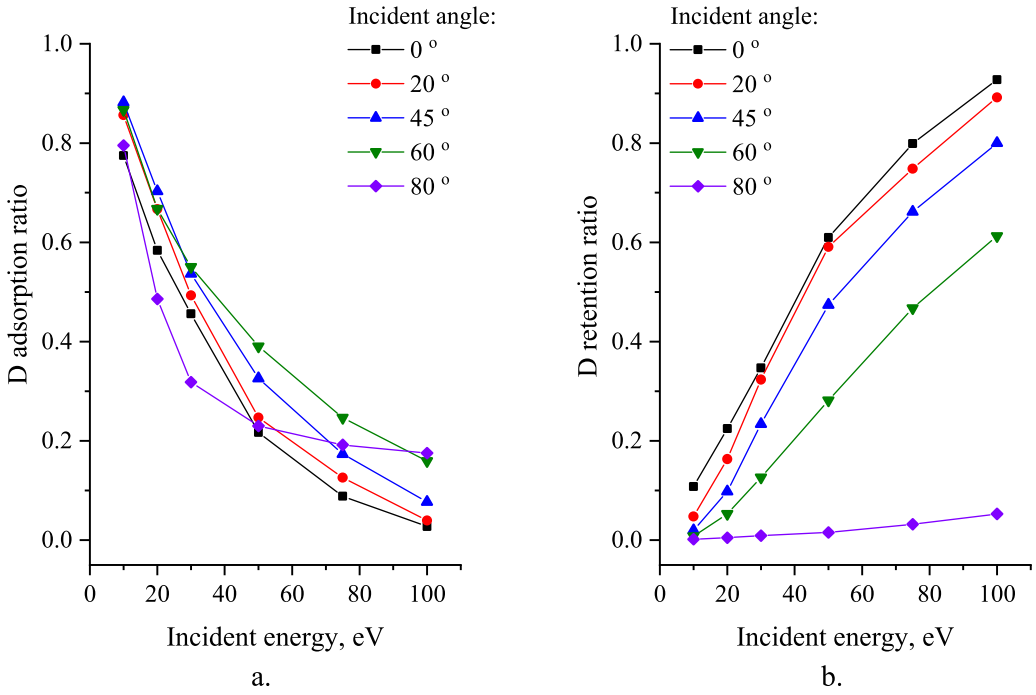

Figure 8. Ratios of D adsorption (*a*) and retention (*b*).

An analysis of the reflected D energy distribution can be summarized such that with increasing impact energy the picture of an elastic reflection very approximately holds, both for the energies ($E_{\text{incoming}} \approx E_{\text{reflected}}$) and the angles (mirroring: $\angle_{\text{incoming}} \approx \angle_{\text{outgoing}}$), but in the low energy range the distributions have a much larger variance.

D atoms that are not reflected remain adsorbed on or penetrate below the surface. Opposed to reflection, penetration of D increases with increasing impact energy. Again, histograms for the other impact energies and other incident angles do not change the discussion and are shown in figures S4 and S5 of the supplementary information.

4.3. D retention and adsorption

In table 1, the events are differentiated into reflection and retention. The last one can have the meaning of retention on the surface (surface adsorption) or retention in the bulk. We base this division on the z-coordinate of the D atom at the end of the simulation. The mutual probabilities are shown in figure

8. As can be seen from the plots, the two parts behave opposite to each other. At lower impact energies, adsorption is prevailing for all angles and reflection processes are negligible. Additionally, at 80°, even at higher energies, the penetration of D into the bulk structure is negligible and surface adsorption dominates.

5. Summary

Be sputtering yields, for varying impact energy and angles, were calculated by non-cumulative MD simulations based on high dimensional neural network potentials. Sputtering simulations of a Be(0001) surface by D impacts with kinetic energy ranging from 10 to 100 eV. The sputtering yield is around 0.03 for incident energies above or equal to 50 eV, which compares very well with literature data using a BOP force field and well comparable with different experimental measurements. The yield decreases rapidly for lower incident energies. The angular dependence of the sputtering yield can be rationalized by a competition between two types of collision cascades as discussed above, where the one characterized by backscattering (S_{II}) causes the information of the angle of the incoming particle to be lost. The retention and reflection probabilities of D behave opposite to each other. At lower energies retention on the surface dominates while with increasing in impact energy and incident angle reflection prevails. Similarly, D retention becomes more frequent with increasing incident energy.

Acknowledgement

This work was partially funded by the Austrian Science Fund, project P28979-N27. L C is grateful for support from the Tyrolean Science Fund (TWF) under project UNI-0404/2308 and from the 'Kommission zur Koordination der Kernfusionsforschung der ÖAW' (KKKÖ). The work has partially been carried out within the framework of the EUROfusion Consortium. M P and L C have received funding from the Euratom research and training programme 2014–2018 and 2019–2020 under Grant Agreement No. 633053. S S has received funding from the European Union's Horizon 2020 research and innovation programme under the Marie Skłodowska-Curie Grant Agreement No. 847476. The views and opinions expressed herein do not necessarily reflect those of the European Commission. The computational results have been obtained using the HPC infrastructure LEO of the University of Innsbruck and the Vienna Scientific cluster VSC3.

ORCID iDs

Lei Chen https://orcid.org/0000-0003-4233-5936
Michael Probst https://orcid.org/0000-0003-3112-5597

References

[1] Brezinsek S. *et al* 2013 *Nucl. Fusion* **53** 083023
[2] Neu R. *et al* 2011 *Plasma Phys. Control. Fusion* **53** 124040
[3] Brezinsek S. *et al* 2017 *Nucl. Fusion* **57** 116041
[4] Pitts R.A. *et al* 2011 *J. Nucl. Mater.* **415** 957–64
[5] Bykov I. *et al* 2016 *Nucl. Instrum. Methods Phys. Res.* B **371** 370–75
[6] Tynan G.R., Baldwin M., Doerner R., Hollmann E., Nishijima D., Umstadter K. and Yu J. 2010 *AIP Conf. Proc.* **1237** 78–91
[7] Skinner C.H. *et al* 2008 *Fusion Sci. Technol.* **54** 891–945
[8] De Temmerman G. *et al* 2021 *Nucl. Mater. Energy* **27** 100994
[9] Roth J., Eckstein W. and Guseva M. 1997 *Fusion Eng. Des.* **37** 465–80
[10] Nishijima D., Doerner R.P., Baldwin M.J. and De Temmerman G. 2009 *J. Nucl. Mater.* **390–391** 132–35
[11] Hakola A. *et al* 2020 *Phys. Scr.* T **171** 014038
[12] Eckstein W., Garciá-Rosales C., Roth J. and László J. 1993 *Nucl. Instrum. Methods Phys. Res.* B **83** 1–2
[13] Eckstein W. 2007 Sputtering yields *Sputtering by Particle Bombardment* (*Topics in Applied Physics* Vol 110) (Berlin: Springer)
[14] Björkas C., Vörtler K., Nordlund K., Nishijima D. and Doerner R. 2009 *New J. Phys.* **11** 123017
[15] Björkas C., Henriksson K.O.E., Probst M. and Nordlund K. 2010 *J. Phys.: Condens. Matter* **22** 352206
[16] Björkas C., Juslin N., Timko H., Vörtler K., Nordlund K., Henriksson K. and Erhart P. 2009 *J. Phys.: Condens. Matter* **21** 445002
[17] Björkas C., Borodin D., Kirschner A., Janev R.K., Nishijima D., Doerner R. and Nordlund K. 2013 *Plasma Phys. Control. Fusion* **55** 074004
[18] Björkas C. and Nordlund K. 2013 *J. Nucl. Mater.* **439** 174–79
[19] Nordlund K., Björkas C., Ahlgren T., Lasa A. and Sand A.E. 2014 *J. Phys. D: Appl. Phys.* **47** 224018
[20] Sukuba I., Kaiser A., Huber S.E., Urban J. and Probst M. 2017 *J. Mol. Model.* **23** 203
[21] Safi E., Björkas C., Lasa A., Nordlund K., Sukuba I. and Probst M. 2015 *J. Nucl. Mater.* **463** 805–809
[22] Safi E., Valles G., Lasa A. and Nordlund K. 2017 *J. Phys. D: Appl. Phys.* **50** 6967
[23] Horsfield A.P., Bratkovsky A.M., Fearn M., Pettifor D.G. and Aoki M. 1996 *Phys. Rev.* B **53** 12694
[24] Ono T., Kenmotsu T. and Muramoto T. 2008 Simulation of the sputtering process *Reactive Sputter Deposition* (*Springer Series in Materials Science* Vol 109) ed D. Depla and S. Mahieu (Berlin: Springer)
[25] Weissmann R. and Behrisch R. 1969 *Radiat. Eff.* **19** 69–75
[26] Behler J. and Parrinello M. 2007 *Phys. Rev. Lett.* **98** 146401
[27] Paleico M.L. and Behler J. 2020 *J. Chem. Phys.* **153** 054704
[28] Ghorbanfekr H., Behler J. and Peeters F.M. 2020 *J. Phys. Chem. Lett.* **11** 7363–70
[29] Weinreich J., Römer A., Paleico M.L. and Behler J. 2020 *J. Phys. Chem.* C **124** 12682–95
[30] Chen L., Sukuba I., Probst M. and Kaiser A. 2020 *RSC Adv.* **10** 4293–9
[31] Chen L., Kaiser A., Probst M. and Shermukhamedov S. 2020 *Nucl. Fusion* **61** 016031
[32] Singraber A., Behler J. and Dellago C. 2019 *J. Chem. Theory Comput.* **15** 1827–40
[33] Singraber A., Morawietz T., Behler J. and Dellago C. 2019 *J. Chem. Theory Comput.* **15** 3075–92
[34] Hohenberg P. and Kohn W. 1964 *Phys. Rev.* **136** B864–71
[35] Kohn W. and Sham L.J. 1965 *Phys. Rev.* **140** A1133–8
[36] Perdew J.P., Burke K. and Ernzerhof M. 1996 Generalized gradient approximation made simple *Phys. Rev. Lett.* **77** 3865–8
[37] Kresse G. and Hafner J. 1993 *Phys. Rev.* B **47** 558–61
[38] Kresse G. and Hafner J. 1994 *Phys. Rev.* B **49** 14251–69
[39] Adolph B., Furthmüller J. and Bechstedt F. 2001 *Phys. Rev.* B **63** 125108
[40] Plimpton S. 1995 *J. Comput. Phys.* **117** 14251–69
[41] Behler J. 2011 *J. Chem. Phys.* **134** 074106
[42] Imbalzano G., Anelli A., Giofré D., Klees S., Behler J. and Ceriotti M. 2018 *J. Chem. Phys.* **148** 241730

[43] Nosé S. 1984 *J. Chem. Phys.* **81** 511–9
[44] Hoover W.G. 1985 *Phys. Rev.* A **31** 1695–7
[45] Stukowski A. 2009 *Modelling Simul. Mater. Sci. Eng.* **18** 015012
[46] Eckstein W. 2002 Calculated sputtering, reflection and range values *IPP Reports* **9/132** 1–132
[47] Meluzova D.S., Babenko P.Y., Shergin A.P., Nordlund K. and Zinoviev A.N. 2019 *Nucl. Instrum. Methods Phys. Res.* B **460** 4–9
[48] Hodille E.A., Byggmästar J., Safi E. and Nordlund K. 2019 *J. Phys.: Condens. Matter* **31** 185001
[49] Allouche A. 2008 *Phys. Rev.* B **78** 085429